Density-Graded Cellular Aluminum**

By *Alan H. Brothers* and *David C. Dunand**

Open-cell metallic foams with controlled, continuous density gradients were created from poly-urethane foam precursors using an investment casting method. This method, designed to improve mass-efficiency in load-bearing metallic foams and facilitate bonding of foams to dense materials in higher-order structures, is described in detail, and demonstrated through pure aluminum foams with model relative density gradients. Methods for structural characterization, including non-destructive local density mapping, are also illustrated.

1. Introduction

Conventional metallic foam processing seeks to maximize uniformity in pore size, relative density, and other aspects of foam structure in order to minimize property variation associated with the statistical nature of foams, and thereby increase their reliability in service.[1,2] However, property uniformity is in many cases an inefficient approach to meeting overall design criteria, as demonstrated by the nonuniform structures of many naturally-occurring porous materials (e.g., bone and wood), as well as by advances from the field of functionally-graded materials (FGM).[3] Recently, the potential of density-graded foam structures was demonstrated explicitly by Daxner et al.,[4] who showed that spatially-varying relative densities led to improved mass efficiency even in fairly simple load-bearing foam components.

Several methods have been developed over the last decade for processing of functionally-graded composite materials, some of which include as intermediate steps the production of density-graded ceramic foams, which are later infiltrated by metals to form graded interpenetrating composites (IPC).[5,6] Other methods have been developed for processing of graded porous ceramics directly, without any metallic matrix.[7–11] These methods generally, however, include processing steps that are not easily extended to metals, and literature pertaining to density-graded metallic foams is therefore comparatively sparse. Though several general methods exist for density-graded porous metals,[6,12] only a few are suited specifically to metallic foams (i.e., with porosity in excess of 50–60 vol.%); the latter have been demonstrated for Cu,[13,14] Ni,[15] Mg,[16] and Al-based[17] metallic foams. However, a general feature of these methods is the production of stepwise, discontinuous density gradients, which are likely to be accompanied by higher flaw densities and/or property

incompatibilities in the interfacial regions separating adjacent uniform-density layers.

In this work, we describe a new method for production of metallic foams having density gradients which are both controllable and continuous. The method, based on replication of density-graded polymer foams through investment casting, shares an initial step with the approach introduced by Cichocki et al.[11] for production of graded porous ceramics, but varies substantially in its later steps and in the porosity and structure of the final products. Though the method is only demonstrated here using simple graded aluminum struc-

[*] A. H. Brothers, Prof. D. C. Dunand
Department of Materials Science and Engineering
Northwestern University
Evanston, IL 60208, USA
E-mail: dunand@northwestern.edu

RESEARCH NEWS

tures, it can be easily extended – within reasonable limits of experimental practice – to the production of graded structures having a range of pore sizes and average densities, arbitrarily-defined density gradients, and a variety of base metals. In what follows, the method is described in detail, together with techniques for characterizing structural parameters such as strut shapes/orientations, flaws, and density gradients.

2. Materials and Methods

A schematic representation of the method for processing of continuously-graded open-cell metallic foams is shown in Figure 1. The starting material is uniform-density, open-cell, elastomeric foam, which is cut into a precursor with a shape determined by the shape and density profile of the final component. The relative density profile itself is arbitrary, provided that: (a) its minimum value is at least the relative density of the precursor (unless a tensile precursor deformation can be applied); and (b) its maximum value is not high enough that precursor densification interferes with later processing steps, e.g. investment filling and removal. The precursor is elastically compressed into the final specimen dimensions (e.g., a uniform cylinder if the precursor has radial symmetry; or a parallelepiped if the precursor has the shape of a wedge or pyramid), generating internal density gradients in the precursor that reflect the strain gradients applied during deformation. The gradient-compressed precursor is then invested with ceramic slurry and removed by pyrolysis. The molten metal is cast into the resulting negative mold, which is then removed, leaving a replica of the deformed and graded precursor foam. In principle, any investment-castable alloy can be used in the final step, provided a compatible investment exists.

The precursor used in this work was commercial reticulated polyurethane (PU) foam with approximate relative density of 2.3 % and pore size of 4–5 mm. Foam precursors were cut with a hot wire apparatus into truncated cones, with one base having diameter equal to the desired final diameter (16 mm) and the opposite base having a diameter larger by a factor $\sqrt{2}$ (22.6 mm); the height of the cone was set to the desired gauge length (25–30 mm). In this way, a simple density profile varying monotonically between the original precursor density (ρ_o = 2.3 %) and twice the precursor density (2 ρ_o = 4.6 %) was generated. This gradient, though not strictly linear due to the square-dependence of density on precursor diameter, gives a near-linear profile with average density 1.55 ρ_o = 3.6 %).

Precursors were coated with a commercial plaster-wetting agent (Rio, Albuquerque NM, USA) to minimize air entrapment during investment, dried, and inserted into oil-lubricated glass tubes with 16 mm inner diameter. This process was done carefully to avoid frictional distortion along the precursor/tube interface and to minimize expansion of the precursor along the axis of the tube. The compressed, graded precursors were invested with plaster (Satin Cast 20, Kerr Lab, Albuquerque NM, USA) and pyrolyzed by slow heating to 500 °C in naturally-convecting air at a rate of ca. 2 °C/min. The resulting plaster molds were placed in graphite-coated quartz crucibles and pressure-infiltrated with 99.7 % pure aluminum at 750 °C using 50 kPa gauge pressure of argon gas. After furnace cooling, infiltrated molds were disintegrated by repeated water quenching from 400–450 °C.

Foam samples were characterized by optical and scanning electron microscopy, as well as 3D micro-computed tomography (μCT) at the Advanced Photon Source of Argonne National Laboratories (Argonne IL, USA). Tomographic reconstruction was achieved using a series of 1500 radiographs, spaced evenly within one 180° half-rotation of a graded foam sample, taken with a monochromatic 30 keV synchrotron x-ray beam with ca. 15 mm width. Details of 3D tomographic reconstruction and analysis of foams can be found elsewhere.[18,19] Foam samples were also analyzed by a simpler technique consisting of radiographic imaging via a white x-ray source operating between 25–60 kV. Samples were imaged in both the stationary state and during rotation about their long axes. In the latter case the period of sample rotation (ca. 0.3 s) was much smaller than the total exposure time (8 min).
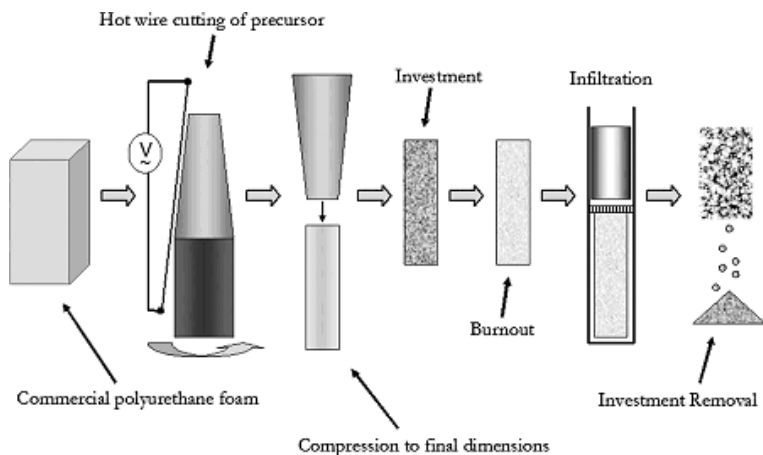
3. Results and Discussion

3.1. Structure

Images of a graded foam sample processed by the described method are shown in Figure 2. The gradient in foam density is difficult to visualize directly in a side view (Fig. 2(a)), but can be recognized through differences in pore size and shape near the sample faces (Fig. 2(b,c)). General foam structure in the undeformed and deformed precursor regions (i.e. the low- and high-density sample faces) is illustrated with greater magnification in

Fig. 1. Schematic illustration of the replication method developed for production of continuously-graded metallic foams.

(Figure labels: Hot wire cutting of precursor; Investment; Infiltration; Commercial polyurethane foam; Burnout; Investment Removal; Compression to final dimensions)
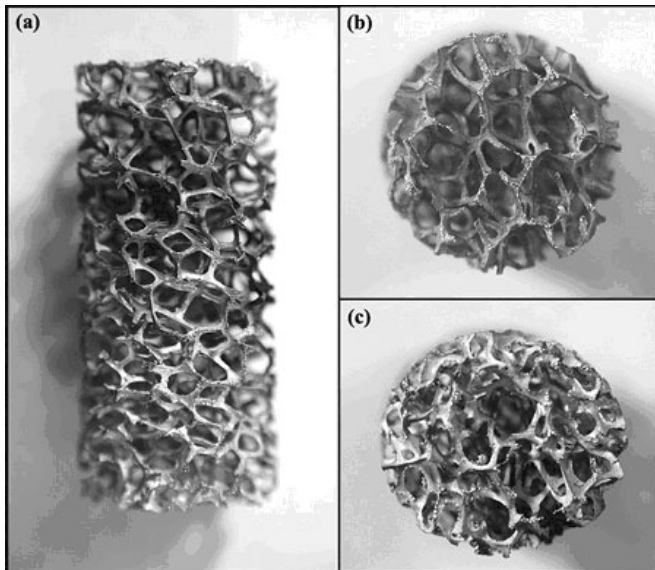
Fig. 2. Photographs of a graded aluminum foam sample processed by the method illustrated in Figure 1. (a) side view, with the low-density face at the top of the panel and the high-density face at the bottom; (b) end view of the low-density face; (c) end view of the high-density face. The diameter of the foam is ca. 14 mm.

Figure 3(a-d). Strut and pore architecture in the undeformed region (Fig. 3(a)) was similar to that of the precursor, with concave-triangular strut cross sections and relatively straight struts (Fig. 3(b)); by contrast, the deformed region (Fig. 3(c)) showed evidence of elastomeric precursor deformation in the form of strut buckling, twisting, and rotation (Fig. 3(d)).

Several types of flaws were visible in the structure, most commonly replicated air bubbles trapped during investment pouring (Fig. 3(e)) and, rarely, regions of incomplete infiltra-
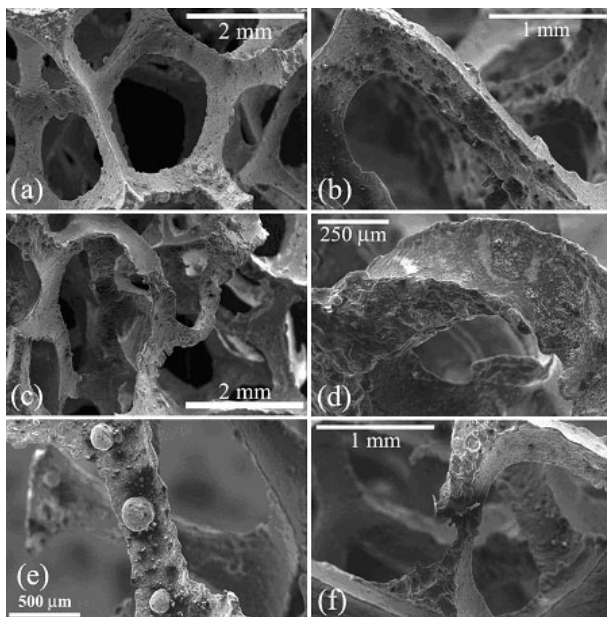

Fig. 3. Scanning electron micrographs illustrating common structures and defects in graded aluminum foam. (a) pore structure in the low-density region; (b) a typical nearly-straight strut in the low-density region; (c) pore structure in the high-density region; (d) a heavily deformed strut in the high-density region; (e) example of replicated bubbles from imperfect investment settling; (f) example of major strut defect.

tion or other major defects (Fig. 3(f)). Imperfect investment settling and retained plaster also led to increased surface roughness relative to the precursor. Tomographic renderings (Fig. 4) of the low- and high-density faces of the sample in Figures 2 and 3 illustrate that the concentrations of all such defects were higher in the higher-density region (i.e., where the precursor had been compressed), reflecting greater numbers of high-curvature and/or re-entrant regions in the deformed precursor, and attending difficulty in accurate investment and infiltration.

3.2. Density Profiling

Analysis of density profiles was performed radiographically because small sample sizes and surface irregularity made other nondestructive analyses (e.g., Archimedes methods, or measurement of properties, such as moment of inertia, that are sensitive to internal mass distribution) difficult, and because radiography provides structural information (e.g., strut conformations) that is more difficult to access by other methods. Two forms of radiographic analysis were compared in this work, the first being direct imaging using a white x-ray source, the second being 3D micro-tomography using monochromatic synchrotron x-radiation.

In the first method, radiographic images were analyzed according to the absorption equation, $I / I_o = e^{-\mu x}$, where I / I_o is the normalized transmitted intensity for a particular pixel in the image, x is the thickness of aluminum separating the source and detector at this pixel (which is related to the foam relative density through the known sample thickness), and μ is the characteristic x-ray absorption length. Strictly, a single value of μ cannot describe transmission of a white x-ray beam in this equation, as μ is energy-dependent and this leads to 'beam hardening.' Nonetheless, an adequate effective value of μ can be determined for a given experiment using an appropriate series of stacked foils, a wedge, or other standard of known and varying thickness. The effective value of μ in this work was determined using a layered aluminum foil standard imaged alongside each sample, giving reproducible values around $\mu = 300$ m^{-1} in all samples.
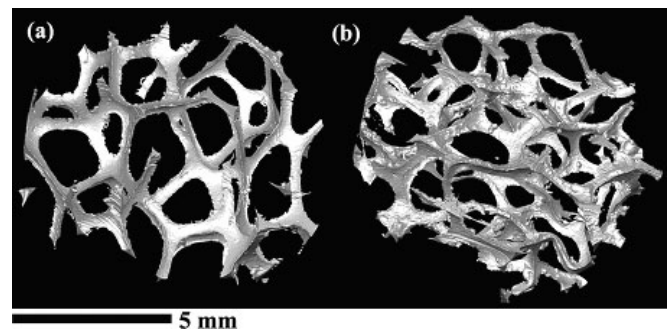

Fig. 4. Tomographic renderings of selected volumes from the graded sample in Figures 2 and 3, taken near: (a) the low-density face; and (b) the high-density face. The scale bar is approximate.

Radiographs of stationary samples, due to low foam density and sample size/cell size ratio, contained many pixels with direct line-of-sight to the x-ray source. Noise in these pixels sometimes led to intensities $I > I_o$, giving spurious negative path lengths that diminished overall accuracy. Rotating samples about their long axes during longer collection times reduced this noise and ensured that all pixels showed $I < I_o$, improving the accuracy of the density calculation. Radiographs of the sample from Figures 2–4, both stationary and rotating, are shown in Figure 5(a) and 5(b).
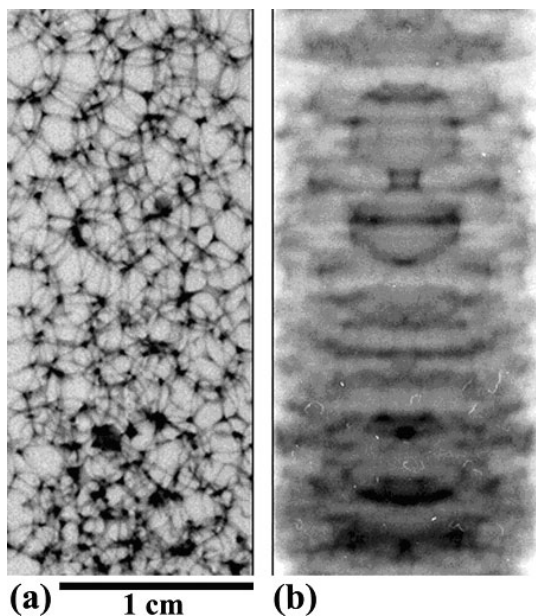

Fig. 5. Radiographic images of the graded foam sample of Figures 2–4, with the low-density face at the top of the panel and the high-density face at the bottom. (a) radiograph of the stationary sample; (b) radiograph of the rotating sample. Radiographs have been contrast-enhanced for better visualization.

The mean relative density of each cross-sectional plane was then calculated from radiographs of rotating samples by weighted averaging (taking into account that pixels near the center of the image represented larger sample volumes than those near the edges), giving net density profiles which could be compared to those predicted from initial precursor dimensions to assess the accuracy of the replication process. The profile calculated from the data in Figure 5(b) is shown in Figure 6, along with the predicted profile. The measured profile appears to track the prediction accurately across the entire gauge length of the sample, with large variability that likely reflects the large pore size of the sample, rather than any inherent noise in the measurement (see next paragraph). The overall relative density of the sample calculated from radiographic density profile (Fig. 6) was 3.5 %, while the value from sample mass and dimensions was 3.8 % and the value predicted from the precursor dimensions was 3.6 %. This error is considered acceptable in light of the fact that: (a) large pore sizes made measurement of foam dimensions less precise; and (b) the radiographic value was derived entirely from
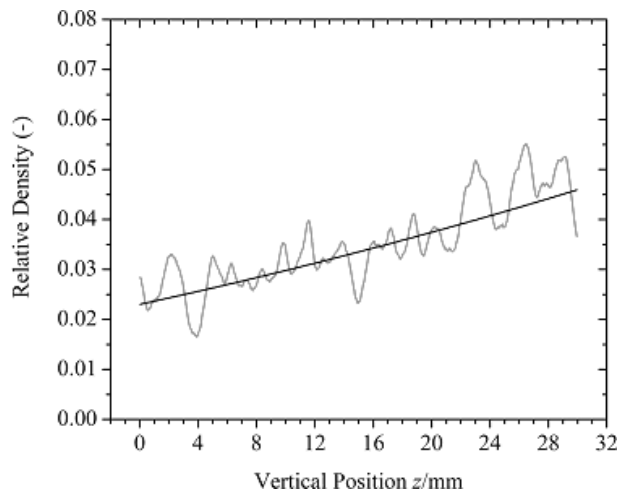

Fig. 6. Relative density profile calculated from the radiographic data in Figure 5(b). Also shown for comparison is the predicted relative density profile estimated from precursor dimensions.

measurements with no assumptions beyond the use of a single representative value of μ.

In the second method, the same sample was analyzed using synchrotron x-ray microtomography (tomographic renderings of the low- and high-density regions of this sample were already presented in Fig. 4). Reconstructed cross-sectional images were binarized and analyzed for area/volume fraction, leading to the density profile shown in Figure 7(a). This profile is in good agreement with the predicted and radiographic profiles (Fig. 6). However, binarization gives the potential for systematic errors in area fraction: experimentation with various thresholding levels led to fluctuations in overall sample density on the order of 0.3 %, sufficient to explain the difference between the calculated density (3.3 %) and the corresponding value (3.5 %) determined by radiography. It is unlikely, however, that binarization fully accounts for the discrepancy with the value determined from physical measurements (3.8 %). Also notable is the fact that the tomographic profile approximately reproduces the prominent features (i.e., larger minima and maxima) of the radiographic profile, confirming that these fluctuations represented real local density fluctuations associated with the large pore size.

Radial density variations (as might occur, for example, if the outermost layer of the precursor were to deform preferentially during reshaping, leaving the inner 'core' relatively undeformed) were investigated by calculating density profiles independently for two roughly equal volumes in the sample, one representing the inner cylindrical 'core' of the sample, the other representing the outermost 'tube.' As shown in Figure 7(b), no consistent density differences were found between these regions. On finer scales (Fig. 7(c)), however, the two density profiles were anti-correlated, indicating that precursor deformation was often localized in one or the other region (that is, either the interior or near-surface region), with the other sustaining less deformation, such that the overall density profile was approximately correct.
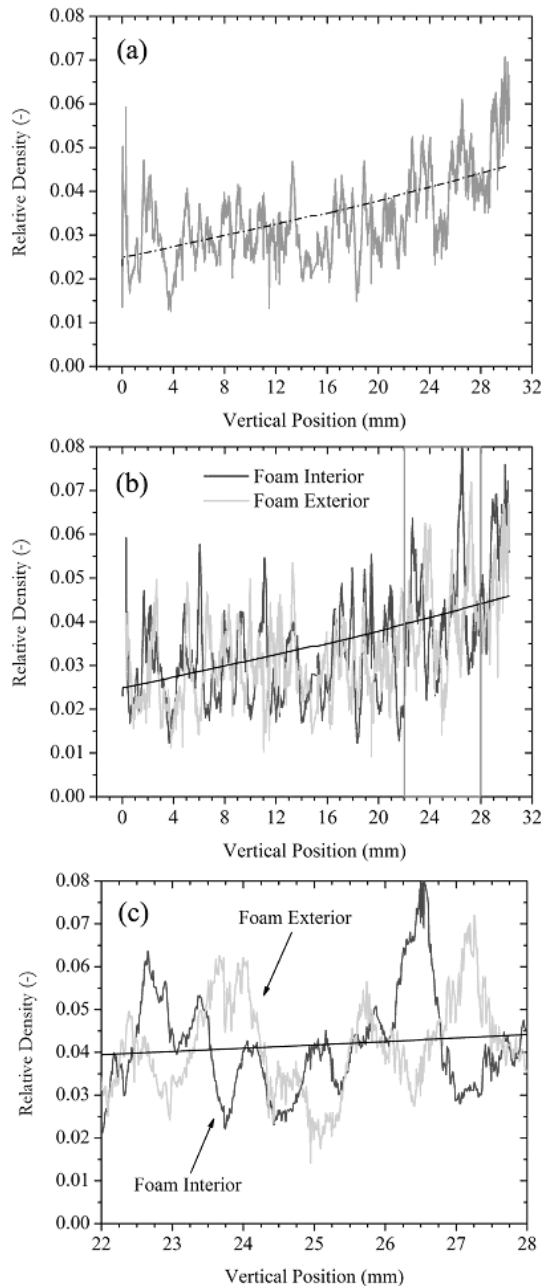
Fig. 7. Relative density profiles calculated from full 3D tomographic data. (a) total relative density profile; (b) relative density profiles plotted separately for the innermost and outermost 50 vol.% of the structure, showing no consistent differences between the near-surface and core regions of the structure; (c) magnified view of the boxed region in panel b, showing local density anti-correlation between the two regions. The predicted profile is shown as a smooth line in each panel for reference.

4. Summary

Foaming methods capable of producing complex, continuous local density gradients have the potential to increase mass efficiency in structural metallic foams, and could help simplify joining/assemblage operations and improve interfacial strength in higher-order structures such as sandwiches. One such method, designed to produce low-density, open-cell graded foams from investment-castable alloys, was introduced here, along with nondestructive techniques for characterizing local density profiles. The method was illustrated by production and structural characterization of graded aluminum foams having simple, near-linear density profiles.

[1] L. J. Gibson, M. F. Ashby, *Cellul. Solids: Struct. and Properties, 2nd ed., Cambridge University Press, Cambridge* **1997**.

[2] M. F. Ashby, A. G. Evans, N. A. Fleck, L. J. Gibson, J. W. Hutchinson, H. N. G. Wadley, *Met. Foams: A Design Guide, Butterworth-Heinemann, Boston* **2000**.

[3] A. Mortensen, S. Suresh, *Int. Mat. Rev.* **1995**, *40*, 239.

[4] T. Daxner, F. G. Rammerstorfer, H. J. Bohm, *Mater. Sci. Technol.* **2000**, *16*, 935.

[5] R. Jedamzik, A. Neubrand, J. Rodel, *J. Am. Cer. Soc.* **2000**, *83*, 983.

[6] S. F. Corbin, X. Zhao-Jie, H. Henein, P. S. Apte, *Mater. Sci. Eng. A* **1999**, *262*, 192.

[7] W. W. Lu, F. Zhao, K. D. K. Luk, Y. J. Yin, K. M. C. Cheung, G. X. Cheng, K. D. Yao, J. C. Y. Leong, *J. Mat. Sci. Mater. Med.* **2003**, *14*, 1039.

[8] J. F. Li, K. Takagi, M. Ono, W. Pan, R. Watanabe, A. Almajid, M. Taya, *J. Am. Ceram. Soc.* **2003**, *86*, 1094.

[9] Y. Kinemuchi, K. Watari, S. Uchimura, *Acta Mater.* **2003**, *51*, 3225.

[10] J. Zeschky, T. Hofner, C. Arnold, R. Weissmann, D. Bahloul-Hourlier, M. Scheffler, P. Greil, *Acta Mater.* **2005**, *53*, 927.

[11] F. R. Cichocki, K. P. Trumble, J. Rodel, J. *Am. Ceram. Soc.* **1998**, *81*, 1661.

[12] M. J. Suk, S. I. Choi, J. S. Kim, Y. D. Kim, Y. S. Kwon, *Met. Mater. Int.* **2003**, *9*, 599.

[13] A. Neubrand, *J. Appl. Electrochem.* **1998**, *28*, 1179.

[14] H. Togashi, K. Yuki, H. Hashizume, *Fusion Sci. Techn.* **2005**, *47*, 740.

[15] C. Solaiyan, P. Gopalakrishnan, S. Dheenadayalan, I. A. Raj, S. Muzhumathi, R. Chandrasekaran, R. Pattabiraman, *Ind. J. Chem. Techn.* **1999**, *6*, 48.

[16] F. W. Bach, D. Bormann, P. Wilk in *Metfoam: 2003*, Verlag MIT Publ. Berlin **2003**.

[17] A. Pollien, Y. Conde, L. Pambaguian, A. Mortensen, *Mater. Sci. Eng.* **2005**, *404*, 9.

[18] A. Elmoutaouakkil, L. Salvo, E. Maire, G. Peix, *Adv. Eng. Mater.* **2002**, *4*, 803.

[19] O. B. Olurin, M. Arnold, C. Korner, R. F. Singer, *Mater. Sci. Eng. A* **2002**, *328*, 334.